A Regional Seasonal Forecast Model of Arctic Minimum Sea Ice Extent: Reflected Solar Radiation vs. Late Winter Coastal Divergence

Rachel Kim

Department of Atmospheric and Oceanic Sciences

McGill University, Montreal

August, 2020

A thesis submitted to McGill University in partial fulfillment of the requirements of the degree of

Master of Science

Dedication

I dedicate my thesis to my partner KL for his generous support, love and companionship that guided me through the two years of graduate school.

Acknowledgements

Abstract

Thinning sea ice cover in the Arctic is associated with larger interannual variability in the minimum Sea Ice Extent (SIE). The current generation of forced or fully coupled models, however, have difficulty predicting SIE anomalies from the long-term trend, highlighting the need to better identify the mechanisms involved in the seasonal evolution of sea ice cover. One such mechanism is Coastal Divergence (CD), a proxy for ice thickness anomalies based on late winter ice motion, quantified using Lagrangian ice tracking. CD gains predictive skill through the positive feedback of surface albedo anomalies, mirrored in Reflected Solar Radiation (RSR), during melt season. Exploring the dynamic and thermodynamic contributions to minimum SIE predictability, RSR, SIE and CD are compared as predictors using a regional seasonal sea ice forecast model for July 1, June 1 and May 1 forecast dates for all Arctic peripheral seas. The predictive skill of June RSR anomalies mainly originates from open water fraction at the surface, i.e. June SIE and June RSR have equal predictive skill for most seas. The finding is supported by the surprising positive correlation found between June Melt Pond Fraction (MPF) and June RSR in all peripheral seas: MPF anomalies indicate presence of ice or open water that is key to creating minimum SIE anomalies. This contradicts models that show correlation between melt onset, MPF and the minimum SIE. A hindcast model shows that for a May 1 forecast, CD anomalies have better predictive skill than RSR anomalies for most peripheral seas.

Abrégé

L'amincissement de la couverture de glace de mer dans l'Arctique est associé à une plus grande variabilité interannuelle de l'étendue minimale de la banquise. La génération actuelle de modèles forcés ou entièrement couplés a cependant du mal à prédire les anomalies de l'étendue de la banquise à partir de la tendance à long terme, soulignant la nécessité de mieux identifier les mécanismes impliqués dans l'évolution saisonnière de la couverture de glace de mer. L'un de ces mécanismes est la divergence côtière, un indicateur des anomalies d'épaisseur de glace basé sur le mouvement de la glace à la fin de l'hiver, quantifié à l'aide du suivi des glaces lagrangiennes. La divergence côtière acquiert une compétence prédictive grâce à la rétroaction positive des anomalies d'albédo de surface, reflétées dans le rayonnement solaire réfléchi, pendant la saison de fonte. En explorant les contributions dynamiques et thermodynamiques à la prévisibilité de l'étendue minimale de la glace de mer, le rayonnement solaire réfléchi, l'étendue de la banquise et la divergence côtière sont comparés en tant que prédicteurs à l'aide d'un modèle régional de prévision saisonnière de la glace de mer pour les dates de prévision du 1er juillet, du 1er juin et du 1er mai pour toutes les mers périphériques de l'Arctique. La capacité prédictive des anomalies du rayonnement solaire réfléchi de juin provient principalement de la fraction d'eau libre à la surface. L'étendue de la banquise et le rayonnement solaire réfléchi du mois de juin ont des capacités prédictives égales pour la majorité des mers. Cette découverte est étayée par la corrélation positive surprenante trouvée entre la fraction de la surface de glace recouverte par des mares de fonte et le rayonnement solaire réfléchi de juin dans toutes les mers périphériques: les anomalies de la fraction de la surface de glace recouverte par des mares de fonte indiquent la présence de glace ou d'eau libre qui est essentielle pour créer des anomalies de l'étendue minimale de la banquise. Cela contredit les modèles qui montrent une corrélation entre l'apparition

de la fonte, la fraction de la surface de glace recouverte par des mares de fonte et l'étendue minimale de la banquise. Un modèle rétrospectif montre que pour une prévision du 1er mai, les anomalies de la divergence côtière ont une meilleure capacité de prédiction que les anomalies du rayonnement solaire réfléchi pour la plupart des mers périphériques.

Contents

List of Figures

List of Tables

Chapter 1

Forward

This thesis is presented in a format of a research article that will be submitted to the Journal of Climate in August 2020. This manuscript satisfies the requirements of a Masters thesis as it consists of an extensive review of relevant literature, a data and methods section and a presentation of results and discussion followed by a conclusion. All chapters presented in this manuscript are to be included in the journal submission. The following provides information of the article and the contribution from co-authors.

1.1 Manuscript Information

Title: A Regional Seasonal Forecast Model of Arctic Minimum Sea Ice Extent: Reflected Solar Radiation vs. Late Winter Coastal Divergence
Authors: Rachel Kim [1] and Bruno Tremblay [1]
To be submitted to: Journal of Climate

1.2 Contributions of Co-authors

This research project was carried out in close collaboration between Professor Bruno Tremblay and Rachel Kim. Literature review and analyses involved in this project were carried out by Rachel Kim. The project's methodology and interpretation of results were carried out by both co-authors.

---

[1]Department of Atmospheric and Oceanic Sciences, McGill University, Montreal, Quebec

Chapter 2

Introduction

Since the beginning of the observational era, the Arctic has witnessed large changes in the minimum sea ice extent (SIE), area, thickness and age (multi-year ice fraction in SIE) with long-term trends approximately equal to -12, -14, -11 and -10% per decade, respectively (Comiso, 2012; Kwok, 2018; Maslanik et al., 2011; Rigor and Wallace, 2004). Superimposed on these trends are large interannual variations (Serreze et al., 2007) that make seasonal and decadal forecasting of the minimum SIE a challenge (Stroeve et al., 2014, 2012). This highlights the speed at which the system is changing, the deficiencies in model physics and the need to identify mechanisms that drive summer sea ice melt. These changes in minimum SIE occur mainly in the North American and Eurasian Arctic with the largest minimum SIE loss found in the East Siberian (22%) and Chukchi (17%) seas since 1979 (Onarheim et al., 2018). Since the variability of the minimum SIE is projected to increase as the Arctic transitions from a perennial to a seasonal ice cover (Holland et al., 2011), the challenges faced by the sea ice forecasting community and stakeholders will only increase. Improving the seasonal forecasts and decadal projections of the minimum SIE is of great importance in mitigating the political, economic, environmental and social consequences of a changing Arctic climate.

In an effort to improve SIE forecasting under a rapidly changing Arctic climate, the Study of Environmental Arctic Change (SEARCH) Sea Ice Outlook (SIO) was initiated in 2008 – one year after the drastic all-time record minimum of 2007 – to compare and assess the predictive skill of forecasting models currently in use in the

community. These include statistical, heuristic, coupled sea ice-ocean and fully coupled sea ice-ocean-atmospheric models. An assessment report by SEARCH SIO covering 2008-2013 shows that the ensemble skill of the models is good when the minimum SIE lies on the long-term trend, but have difficulty forecasting the minimum SIE when the annual anomaly is large (Stroeve et al., 2014, 2012).

Model studies also highlight the importance of sea ice thickness and sea surface temperature anomalies in the initialization of seasonal predictions of the minimum SIE (Blanchard-Wrigglesworth et al., 2011; Chevallier and Salas-Mélia, 2012; Guemas et al., 2016; Msadek et al., 2014). For instance, two models with similar ice and ocean components but with different atmospheric components show similar skill in summer SIE forecasts (Msadek et al., 2014). Bushuk et al. (2017b) find a May "barrier of predictability" in the Geophysical Fluid Dynamics Laboratory global climate model; i.e. May or earlier sea ice thickness anomalies in the peripheral seas have no predictive skill of the minimum SIE. On the other hand, Bushuk et al. (2017a, 2020) find using a fully coupled global climate model that sea ice thickness anomalies are amplified between May and July after melt onset by the ice albedo feedback.

This link between sea ice thickness and surface albedo anomalies strengthens as the Arctic transitions from a perennial to a seasonal ice cover because a larger fraction of the ice pack consists of thinner, saltier, weaker and more mobile first-year ice (FYI) that has a lower melting point, a higher surface temperature and a lower surface albedo (Rigor et al., 2002). Due to a more mobile and thinner ice pack, a simplified coupled ice-ocean model showed an increased sensitivity of sea ice anomalies since 2000 to early summer divergent ice motion (Kashiwase et al., 2017). Similarly, Perovich et al. (2008) report a five-fold increase in the heat input to the upper ocean from positive anomalies in early summer open water fraction. Flatter FYI ice also leads to a larger melt pond area compared to ridged multi-year ice (Perovich and Polashenski, 2012). For instance, simulated Melt Pond Fraction (MPF) from an ice-ocean coupled model was found to significantly correlate with the minimum SIE as early as May (Schröder et al., 2014). However, the fact that MPF in the Baffin Bay, Canadian Archipelago and central Arctic beyond the seasonal ice zone contribute to the correlation suggests that MPF may be

correlated with a third parameter physically related to the minimum SIE (e.g. Arctic Oscillation, Williams et al., 2016).

The positive feedback mentioned above that amplify sea ice thickness anomalies through the surface albedo suggest a potential predictability of the minimum SIE from observations (currently absent from physical models). June Reflected Solar Radiation (RSR) is significantly correlated with the September minimum SIE for the pan-Arctic (Choi et al., 2014; Huang et al., 2019; Zhan and Davies, 2017) as surface albedo anomalies become important after melt onset (Kapsch et al., 2016). As such, the predictability of Top-Of-Atmosphere (TOA) RSR is closely related to the contribution from surface anomalies (open water and melt ponds) rather than atmospheric anomalies (clouds, water vapor, aerosols etc.) in June. This link, however, is not as robust for earlier forecasts dates (Kapsch et al., 2016; Zhan and Davies, 2017). The summer cloud effects are also debated. Choi et al. (2014) and Huang et al. (2019) attribute June RSR anomalies to both the cloud shielding effect and surface albedo anomalies while Francis et al. (2005) find no cloud shielding effect with respect to sea ice melt and argues instead that downwelling longwave anomalies in the summer explain most of the variability (approximately 40%) in the minimum SIE in Arctic peripheral seas.

Ultimately, dynamical processes are key to the generation of ice thickness anomalies that are amplified later in summer by thermodynamical processes. The increased mobility of ice cover and sea-ice drift speed since the mid-90s, after large positive Arctic Oscillation index anomalies and associated flushing of multi-year ice out of the Arctic, was an important turning point for late winter coastal divergence as a predictor of the minimum SIE (Maslanik et al., 2007; Rigor and Wallace, 2004; Rigor et al., 2002; Spreen et al., 2011). Thin ice formed from late winter coastal divergence will grow to an approximate thickness of 1.15-1.45 m, the climatological summer melt (Nikolaeva and Sesterikov, 1970). This suggests a potential predictive skill for sea ice melt area the following summer through sea ice thickness anomalies (Brunette et al., 2019; Bushuk et al., 2017a; Chevallier and Salas-Mélia, 2012; Nikolaeva and Sesterikov, 1970; Williams et al., 2016). For instance, Chevallier and Salas-Mélia (2012) report a similar critical sea ice thickness of 0.9-1.5 m that can be used to predict the minimum SIE up to 6 months

in advance using a coupled global climate model. Williams et al. (2016) use late winter dynamic preconditioning area (or coastal divergence) from a Lagrangian ice model forced with observed sea ice drift to develop a skillful statistical model of the minimum SIE. Following Nikolaeva and Sesterikov (1970), Brunette et al. (2019) use a similar Lagrangian approach to skillfully predict the minimum SIE in the Laptev Sea from late winter divergence area.

Other factors with potential predictive skill include cloud longwave forcing and ocean heat transport. Winter cloud forcing anomalies integrated from November to February using reanalysis data explain approximately 25% of the variance in the minimum SIE at a 90% confidence level in the East Siberian and Kara seas, suggesting a potential predictive skill of winter radiative flux anomalies for the minimum SIE (Letterly et al., 2016). Liu and Key (2014) and Letterly et al. (2016) report on similar spatial patterns between September SIE anomalies and winter cloud anomalies integrated from January to February and November to February (respectively) and advected until September using Polar Path Finder sea ice drift data. These results, however, may be circumstantial as both studies look at only one signature year, 2013 and 2007, and use summer sea ice drift that comes with increased uncertainty compared to that in winter (Tschudi et al., 2019b). Similarly, Cao et al. (2017) merges in-situ observation and reanalysis data to find similar spatial patterns between winter downward longwave radiative forcing anomalies and SIC anomalies during melt onset (mid-May to early June) but only looks at two anomalously low (1990, 2006) and high (1999, 2013) melt onset years without considering a link with the minimum SIE. Kapsch et al. (2016) uses a fully coupled global climate model to report that winter cloud forcing has negligible influence and rather spring and early summer cloud forcing have an influence on the following September SIE. Finally, ocean heat transport through the Bering Strait is suggested to influence late summer anomalous sea ice conditions by triggering the onset of sea ice melt (Woodgate et al., 2010). Using in-situ mooring observations, the sea ice retreat date in the Chukchi Sea was found to correlate most strongly with Bering Strait ocean heat transport from April to June (Serreze et al., 2016). On decadal timescales, a study from the Community Earth System Model Large Ensemble showed that rapid declines in SIE were mainly correlated

with ocean heat transport through the Bering Strait and the Barents Sea opening where sea ice cover lies over shallow continental shelves that allow ice-ocean interaction to dominate (Auclair and Tremblay, 2018).

Building on the fact that sea ice thickness anomalies are at the origin of predictability of RSR and can be preconditioned by late winter dynamics, this study focuses on the regional and seasonal minimum SIE predictability and in particular on the three following questions: 1. What fraction of June RSR anomalies comes from open water fraction, MPF and atmospheric contribution? 2. Can late winter coastal divergence lead to longer lead-time with comparable predictive skill to that of June RSR? 3. If so, by how much can we increase the forecast lead-time from late winter coastal divergence, if at all, for all Arctic peripheral seas?

This study presents a statistical seasonal forecast model based on observations for five Arctic peripheral seas: the Beaufort, Chukchi, East Siberian, Laptev and Kara. First, we find that June SIE anomalies are equally or more skillful than June RSR anomalies for the seasonal forecast of the minimum SIE for all seas. The Kara Sea stands as an exception since melt ponds and clouds introduce uncertainty in the RSR. Moreover, we find that while June MPF is negatively correlated with RSR in the central Arctic and landfast ice area, it is positively correlated in the peripheral seas. This is because positive anomalies in MPF area are associated with ponded ice that reflect presence of ice to be melted, whereas negative MPF anomalies are associated with negative open water anomalies in the peripheral seas. In May and April, RSR has better predictive skill than SIE in the Laptev Sea since the former reflects albedo variations related to SIT anomalies and atmosphere effects related to polynyas. Finally, we find that lead-time can be extended by 2 months for all peripheral seas from late winter coastal divergence, except for the Laptev Sea, where April RSR shows higher skill than May-1 late winter coastal divergence, and the East Siberian Sea, where neither May-1 late winter coastal divergence and April RSR show skill. For the Kara Sea, late winter coastal divergence shows superior predictive skill for all forecast dates.

This paper is structured as follows: Chapter 3 describes the observational data used in this study: sea ice concentration, radiative fluxes, melt pond fraction, sea ice drift and

ocean heat transport through the Bering Strait. The Lagrangian Ice Tracking System (LITS) used for tracking sea ice and quantifying late winter coastal divergence is also described in Chapter 3. In Chapter 4, we first identify the sources of predictability in RSR: open water fraction, melt pond fraction and atmospheric components. In the same chapter, we compare predictive skill of RSR, SIE and late winter coastal divergence for each peripheral sea. Finally, we present hindcast models using the linear trend, RSR and late winter coastal divergence as predictors for each peripheral sea. Conclusion and future work are summarized in Chapter 5.

Chapter 3

Data and Methods

3.1 Data

3.1.1 Sea Ice Concentration

We use the Daily NOAA/NSIDC Climate Data Record of Passive Microwave Sea Ice Concentration (SIC) Version 3 from July 1987 to December 2018 available on the 25 km $\times$ 25 km Equal-Area Scalable Earth (EASE) Grid (Meier et al., 2017; Peng et al., 2013). SIC is the percentage of ocean area covered by sea ice. The data is derived using brightness temperatures from the Defense Meteorological Satellite Program (DMSP) Special Sensor Microwave/Imagers (SSM/I) and DMSP Special Sensor Microwave Imager/Sounder (SSMIS). We calculate the weekly and monthly SIC from the daily SIC data. The error is approximately 5% and up to 20% in winter and summer compared to airborne or satellite remote sensing data of higher resolution than SSM/I and SSMIS instruments (Meier et al., 2017; Steffen et al., 1992). The higher error in summer are due to clouds and sea ice surface melt effects on the measured brightness temperatures (Meier et al., 2011, updated 2017). We define Sea Ice Extent (SIE) as the total area of all grid cells with SIC $\geq$ 15 %.

3.1.2   Radiative Flux

We use the gridded monthly mean Top-Of-Atmosphere (TOA) all-sky and clear-sky reflected solar radiation (RSR) and all-sky surface longwave downwelling (LWD) flux from the Clouds and the Earth's Radiant Energy System (CERES) Energy Balanced and Filled (EBAF) Edition 4.1 (Kato et al., 2018; Loeb et al., 2018). CERES instruments are on the Terra and Aqua satellites and provide daily data coverage at a global scale with a spatial resolution of $1° \times 1°$ from March 2000 to present (CERES Science Team, 2018).

TOA all-sky radiative fluxes are corrected using global mean energy budget constraints derived from in-situ Argo observations (Loeb et al., 2009). CERES EBAF clear-sky TOA fluxes are corrected using a radiative transfer model that removes clouds but is initialized with identical properties to all-sky conditions such as surface temperature, temperature/humidity profiles, aerosols and surface albedo. Satellite-based clear-sky fluxes are derived from cloud-free regions within a grid box and are weighted according to the cloud fraction identified by applying a cloud mask of higher resolution (Loeb et al., 2020). TOA-RSR is chosen over surface RSR since TOA irradiance is directly derived from satellite measurements with uncertainties of 2.5 and 5.4 W/m^2 for all-sky and clear-sky, respectively. Surface irradiance has a higher uncertainty of 11 W/m^2 (all-sky and clear-sky) as errors are introduced from input sources of satellite-derived cloud and aerosol properties, and temperature and specific humidity profiles from reanalysis (Kato et al., 2018; Loeb et al., 2020). Moreover, Choi et al. (2014) compared the previous version of CERES TOA and surface radiative flux anomalies and report that absorption and scattering by the atmosphere have minor effects on the absorbed solar radiation.

Monthly mean all-sky surface LWD fluxes are derived from CERES SYN 1-deg-Month, which gives gridded monthly mean surface fluxes computed using cloud properties from MODIS and geostationary satellites (CERES Science Team, 2020). All-sky surface LWD fluxes are used instead of clear-sky in order to focus on winter cloud preconditioning effects on sea ice. For surface LWD fluxes, error is introduced from the bias in the computed cloud fraction viewed from the surface, which is corrected

using CALOPSO/CLOUDSat, MODIS and geostationary satellites (CERES Science Team, 2020). The degradation of the Terra MODIS water vapor channel that affects night time cloud mask over polar regions (60°N to 90°N) causing a downward trend in LWD anomalies is also corrected starting in January 2003 to match the cloud fraction derived from the Aqua satellite (CERES Science Team, 2020). The overall uncertainty for surface LWD is 9 W/m^2 (Loeb et al., 2020) and is larger for polar regions (12 W/m^2 CERES Science Team, 2020).

3.1.3 Melt Pond Fraction

We use Integrated Climate Data Center (ICDC) "clear-sky" Melt Pond Fraction (MPF) data Version 2 available in 8-day composites from May 9 to September 13 for the time period 2000-2011 at a spatial resolution of 12.5 $\times$ 12.5 km (Rösel et al., 2012). The data set provides the MPF per grid cell. MPF is derived using an artificial neural network algorithm on MODIS data at frequency bands 1, 3 and 4 in a grid cell size of 500 m. The neural network uses different surface reflectance values for snow, sea ice, melt ponds and open water. "Almost clear-sky" MPF is defined as 12.5 km grid cells derived from more than 90% usable 500 m grid cells (Rösel et al., 2012). We use clear-sky MPF since all-sky MPF include grid cells derived from a low fraction of usable 500 m grid cells and are flagged (if less than 10%) for increased uncertainty (Rösel et al., 2012). The uncertainty of the derived data is 6% (Rösel et al., 2012). The derived data set was also compared with aerial photos from the Beaufort Sea in 2000, 2001 and 2008 NSIDC data from four sites located throughout the Arctic and ship observations from the trans-Arctic HOTRAX cruise in 2005. The approximate RMSE are 11%, 10.7% and 3.8%, respectively (Rösel et al., 2012).

3.1.4 Sea Ice Drift

We use the Weekly Polar Pathfinder (PPF) Sea Ice Motion Vectors, Version 4 of NSIDC on the 25 km $\times$ 25 km EASE grid from 1993 to 2018 (Tschudi et al., 2019b) in the Lagrangian Ice Tracking System (LITS) (Brunette et al., 2019; DeRepentigny et al., 2016; Williams

et al., 2016). This model is an adapted version of the Sea Ice Tracking Utility (SITU) software (`http://icemotion.labs.nsidc.org/SITU/`). Weekly mean fields are calculated by averaging daily motion vectors. Daily motion vectors are derived using an optimal interpolation scheme to merge the Advanced Very-High-Resolution Radiometer (AVHRR), the Advanced Microwave Scanning Radiometer-Earth Observing System (AMSRE), the Scanning Multi-channel Microwave Radiometer(SMMR), the Special Sensor Microwave Imager/Sounder (SSMIS), and the Special Sensor Microwave/Imager (SSM/I) passive microwave sensors, International Arctic Buoy Program (IABP) buoy data and NCEP/NCAR reanalysis wind (geostrophic wind) data set (Tschudi et al., 2019b). The daily ice motion from satellite imagery is derived using a maximum cross-correlation method (Emery et al., 1995). The optimal interpolation scheme uses weight for each sea ice motion vector based on input source's accuracy and distance, and takes the average of the 15-highest-weighted ice motion vectors. This merged sea ice motion dataset is temporally and spatially complete (Tschudi et al., 2019a). Buoy-excluded merged sea ice motion vectors were compared with buoy data for accuracy assessment. Mean difference between the daily merged vector and buoy data is 0.1cm/s with RMS error of 3.36 cm/sec in the u-component and 0.4 cm/sec with RMS error of 3.40 cm/sec in the v-component (Tschudi et al., 2019b). While a low bias in drift speed between 1978 and 1987 was reported due to a lower temporal sampling of SMMR (Tschudi et al., 2019b), this study uses sea ice drift data from 1993 for all analyses presented and the bias does not affect the results. Lastly, a sea ice mask with a threshold of SIC $\geq$ 15 % is applied to sea ice motion fields to retrieve motion estimates from ice-covered ocean only. Moreover, a land mask is applied to eliminate cells near coasts and within the Canadian Archipelago as motion retrieval is unreliable in these areas due to mixed land, ocean and ice cells (Tschudi et al., 2019a).

3.1.5 Ocean Heat Transport

We use monthly mean ocean heat transport (OHT) data in the time period 1998-2015 from Woodgate (2018). The monthly mean OHT is derived from the A3 mooring deployed 35

km north of the Bering Strait at a depth of 57 m (Woodgate, 2018). The A3 mooring was chosen according to its observation quality, completeness throughout the record period and its proximity to the Bering Strait (Woodgate, 2018). However, the Alaskan Coastal Current is not sampled in the mooring, and this omission results in an underestimation of the Bering Strait transport by approximately 25% (Woodgate, 2018). Despite the underestimation, the Bering Strait OHT data shows a strong correlation in the velocity and temperature measurements with the A4 mooring deployed near the Alaskan coast and hence, provides an accurate measure of the Bering Strait OHT anomalies (Woodgate, 2018). The uncertainty in the OHT estimates is lower than 5% (Woodgate, 2018).

3.2   Methods

We present a regional seasonal forecasting model of the minimum SIE for each peripheral sea of the Arctic Ocean. Following Nikolaeva and Sesterikov (1970), Krumpen et al. (2013), Williams et al. (2016) and Brunette et al. (2019), we use late winter coastal divergence area, hereon referred to as Coastal Divergence (CD), as a predictor of the September minimum sea ice extent. At initialization, LITS places tracers in each 25 km $\times$ 25 km EASE-grid cell over the pan-Arctic domain at a given start week (WX). For each year, tracers are advected with a 1-week time step using the PPF data set from start week (WX) until the last week of April, May and June to produce May 1, June 1 and July 1 forecasts, respectively. At each time step, advected sea ice tracers lying outside the SIC $\geq$ 15% threshold is flagged as inactive and no longer advected. At the end of the integration, we quantify the area of CD with the number of grid cells that are free of tracers in each Arctic peripheral sea (Figure 3.1). The error estimate on the CD area estimate is therefore 625 km^2 (25 km $\times$ 25 km) multiplied by the characteristic length (parallel to the coast) of a peripheral sea.

DeRepentigny et al. (2016) compared sea ice drift simulations from the PPF dataset with IABP buoy data to quantify tracking error in LITS. For a weekly temporal resolution, the median error in trajectories is 7% and the upper-quartile error is 16% of the total distance travelled. The trajectory error is about 25 km and 36 km for a 12-week (from 1st
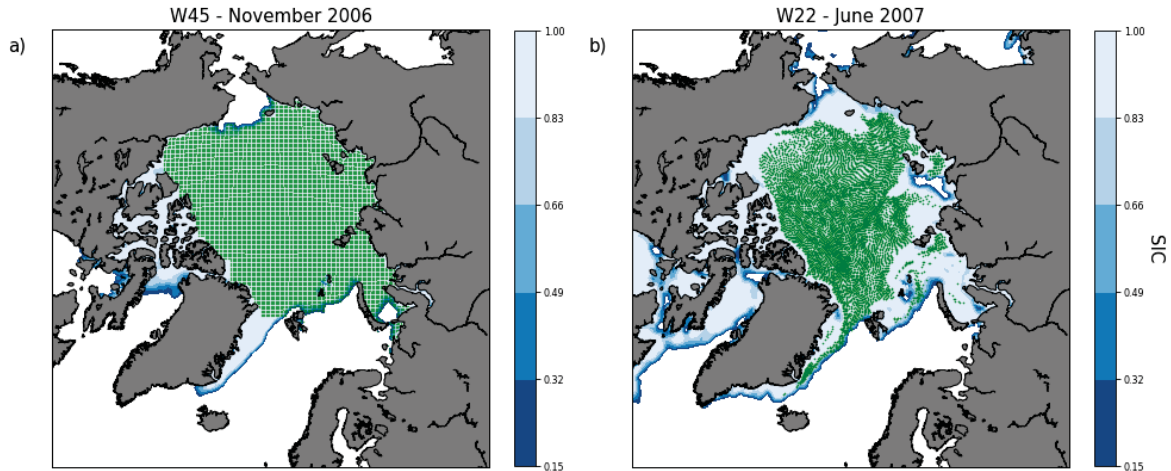
Figure 3.1: a) Initial and b) final positions of sea ice tracers (green dots) advected from the first week of November 2006 (W45) until the last week of June 2007 (W22) using the Lagrangian Ice Tracker System (LITS). Blue shading show the SIC in the background. Note that most of the coastal divergence, inferred from the area with no green dots, in each peripheral sea occurs in late fall and early winter when the pack is more mobile. We show a November 1 start week as an example instead of a late winter start week for the sake of clarity as the signal in coastal divergence is larger.

week of March to 1st week of June) and 17-week (from 1st week of Feb. to 1st week of June) advection, respectively.

Predictability of the minimum SIE is analyzed for each of the Arctic peripheral seas, as defined in NSIDC (ftp://sidads.colorado.edu/DATASETS/NOAA/G02186/ancillary/; see also Figure 3.2). The Barents and East Greenland seas are not included in this study as sea ice is not present in late summer.

All data sets are interpolated on the EASE-grid with a 25-km resolution. We subtract the climatological mean and linearly detrend the data sets to remove seasonal and secular trends in order to focus on the interannual variability. From here on, SIC, SIE, RSR, LWD, MPF and OHT refer to monthly anomalies and CD refer to integrated coastal divergence area anomalies unless specified otherwise. The Pearson correlation coefficients presented in this study are significant at the 95% confidence level, unless specified otherwise.
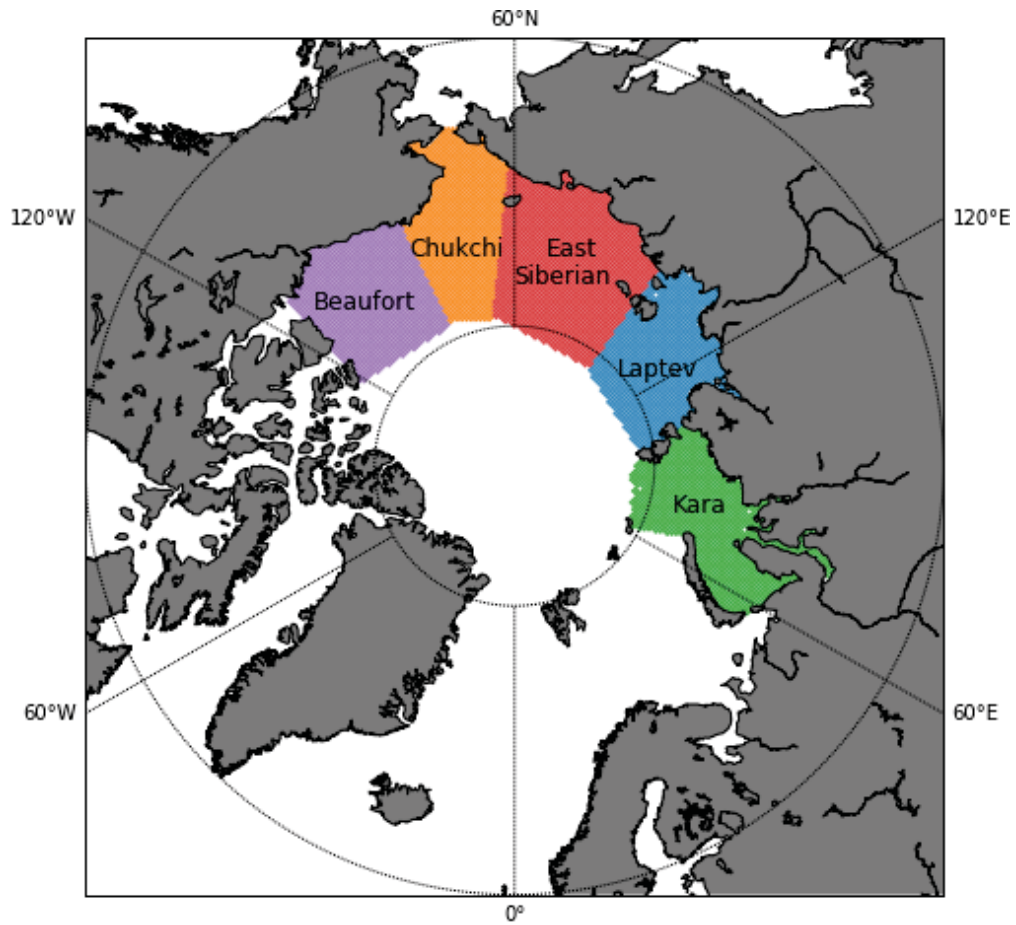
Figure 3.2: Arctic map including the definition of peripheral seas: Beaufort, Chukchi, East Siberian, Laptev and Kara. The jagged edges along each peripheral sea gives an indication of the spatial resolution of the EASE-grid used in this study.

Chapter 4

Results and Discussion

4.1   RSR Variability: Atmosphere vs. Surface

We first aim to quantify sources of predictability in RSR from the atmosphere (water vapor, clouds) and surface conditions (melt pond, open water) for each peripheral sea and forecast lead-time. To this end, we calculate the Pearson correlation coefficients between all-sky RSR and clear-sky RSR, all-sky RSR and all-sky surface LWD, clear-sky RSR and SIC, and clear-sky RSR and clear-sky MPF for June, May and April (Figure 4.1). The first, second, third and fourth columns in Figure 4.1 each indicate the fraction of variance explained by the surface, atmosphere (water vapor, clouds), open water and melt pond, respectively. Clear-sky RSR explains ≈ 60–75% of the variance in all-sky RSR in the peripheral seas where the correlation is significant and SIC variability is above 5% for all forecast dates (Figure 4.1-first column). All-sky LWD is negatively correlated in the Kara and Laptev seas and not correlated in other peripheral seas indicating a positive feedback from the presence of clouds - i.e. low SIC, low RSR and high cloud/LWD. In the central Arctic where SIC variability is low, all-sky LWD explains 25–27% of the variance in all-sky RSR (positively correlated: high cloud, high RSR/LWD), indicating that both surface and atmospheric effects are important in regions of low SIC variability (Figure 4.1 - second column). We conclude that the surface conditions ($r^2 = 0.60$–0.75) dominate the TOA-RSR signal and that the atmosphere, while being non-negligible in certain regions and months, is of less importance, in accord with Zhan and Davies (2017).
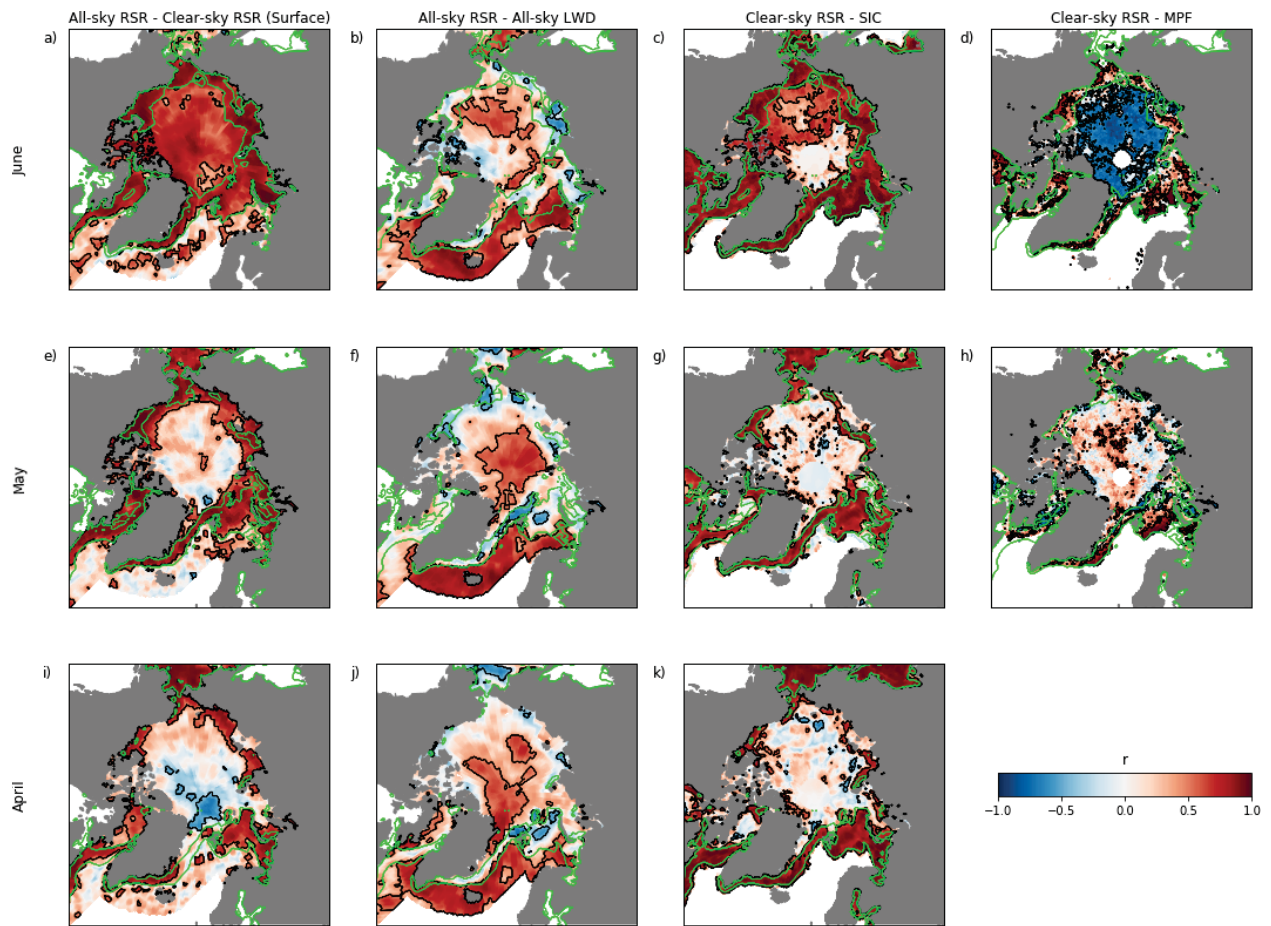
Figure 4.1: Pearson correlation coefficients between detrended June (a-d), May (e-h) and April (i-k) all-sky and clear-sky Reflected Solar Radiation (RSR, first column), all-sky RSR and all-sky surface Longwave Downwelling radiative flux (LWD, second column), clear-sky RSR and Sea Ice Concentration (SIC, third column), and clear-sky RSR and clear-sky Melt Pond Fraction (MPF, fourth column) anomalies for the time period 2000–2018 (RSR, LWD and SIC) and 2001–2011 (MPF). The black outline shows regions with significant correlations at the 95 % confidence level. The green outline shows regions where the SIC variability is greater than 5 % ($\sigma > 0.05$). Clear-sky RSR explains 70%, 74%, 61% of the variance in all-sky RSR. SIC and clear-sky MPF explain 65%, 55%, 61% and 7% (from positive correlation), 23%, 0% (before melt onset) of the variance in clear-sky RSR in June, May and April, respectively, in the five peripheral seas, where the correlation is significant at the 95% confidence level (black outline) and SIC variability is greater than 5% (green outline).

The surface conditions can be broken into two parts: melt pond and open water fraction. In the peripheral seas where the correlations are significant and interannual variability of SIC is above the 5% threshold, open water fraction explains 55–65% of the variance in April–June clear-sky RSR while clear-sky MPF explains 7% (positive correlations) in clear-sky June RSR, 23% (i.e. a larger fraction) in clear-sky May RSR when melt ponds start to form (Kwok et al., 2003, see Figure 3: centre, right column) and 0% in clear-sky April RSR prior to melt onset. Note that MPF derived under all-sky conditions does not correlate with all-sky RSR in June ($r^2 = 0.01$) nor May ($r^2 = 0.00$) for any of the peripheral seas. The fact that the correlation between MPF and clear-sky RSR is only apparent in the clear-sky MPF product indicates that open water dominates the surface signal, and MPF and atmosphere conditions are two signals of equal importance competing with one another. Note that while open water fraction (SIC) explains most of the variance in clear-sky RSR for all months, the area over which the variability of SIC is above the threshold ($\sigma > 5\%$) decreases from June (when it covers most of the peripheral seas) to May and April when it covers much smaller areas limited to coastal water polynyas (Morales Maqueda et al., 2004; Preußer et al., 2019).

We also note that clear-sky MPF in June is positively correlated with clear-sky RSR in all peripheral seas except over land fast ice in the Laptev Sea, western East Siberian Sea and the central Arctic (Figure 4.1d), where SIC variability is low. The positive correlation in the peripheral seas is counter-intuitive and contradictory to previous studies arguing that MPF is a skillful predictor of the minimum SIE (Bushuk et al., 2020; Liu et al., 2015; Schröder et al., 2014). This suggests again that open water fraction rather than MPF is key for the minimum SIE. In the peripheral seas, positive MPF anomalies mean that ice is actually present at the surface whereas negative anomalies typically mean no ice, as opposed to ice that has little melt pond area. In the central Arctic and over land fast ice, positive MPF anomalies mean more melt pond over ice that typically persists or systematically melts each year. The fact that MPF is positively correlated in regions of the peripheral seas where you have large interannual variability in SIE and negatively correlated in regions where interannual variability is small indicate that "presence of ice"

in peripheral seas, even if ponded, is detrimental to the production of large negative anomalies in the minimum SIE.

In the central Arctic, June MPF still explains 42%of the variance where correlation is significant, but SIC variability is less than 5%. At high latitudes, between 80-88°N, SIC is typically higher, ice is fresher and thicker and therefore less permeable to surface runoff from melt ponds, leading to a maximum MPF per grid cell despite the sun being lower on the horizon (Rösel et al., 2012; Tschudi et al., 2008). Below, we compare the predictive skill of SIE, RSR and CD in light of the results above for all peripheral seas of the Arctic and for all forecast dates.

4.2   RSR, SIE and CD Predictive Skill

For the most part, the predictive skill of RSR and SIE (or equivalently, SIA, not shown) is equal and significant (within uncertainty, see Table A.1) and explain between 25 and 70% of the variance in the minimum SIE for all peripheral seas for the month of June (Figure 4.2). In May and April, they mostly lose their predictive skill in agreement with previous studies showing a loss of early summer SIE's predictability for detrended minimum SIE when forecast lead-times are greater than 3 months (see Figure 4.2 Blanchard-Wrigglesworth et al., 2011; Lindsay et al., 2008). CD is equally skillful as RSR and SIE for a July 1 forecast and remain skillful for June 1 and May 1 forecasts except for the Chukchi and East Siberian seas, where other dynamical and thermodynamical factors are important and divergent ice motion is weak (see Section 4.2.2 and 4.2.3 below). We note that July 1 forecasts are past the melt onset date and as such, the last weeks of tracer advection do not represent late winter dynamic preconditioning but rather early summer dynamic ice loss. This is in part why CD forecasts of the minimum SIE continue to be skillful after melt onset. Lastly, the difference in correlation magnitudes between CD and RSR where both show significance are negligible for each peripheral sea given their uncertainties (Table A.1, Figure B.1)

We now discuss regional predictability for each peripheral sea separately and for all forecast dates.
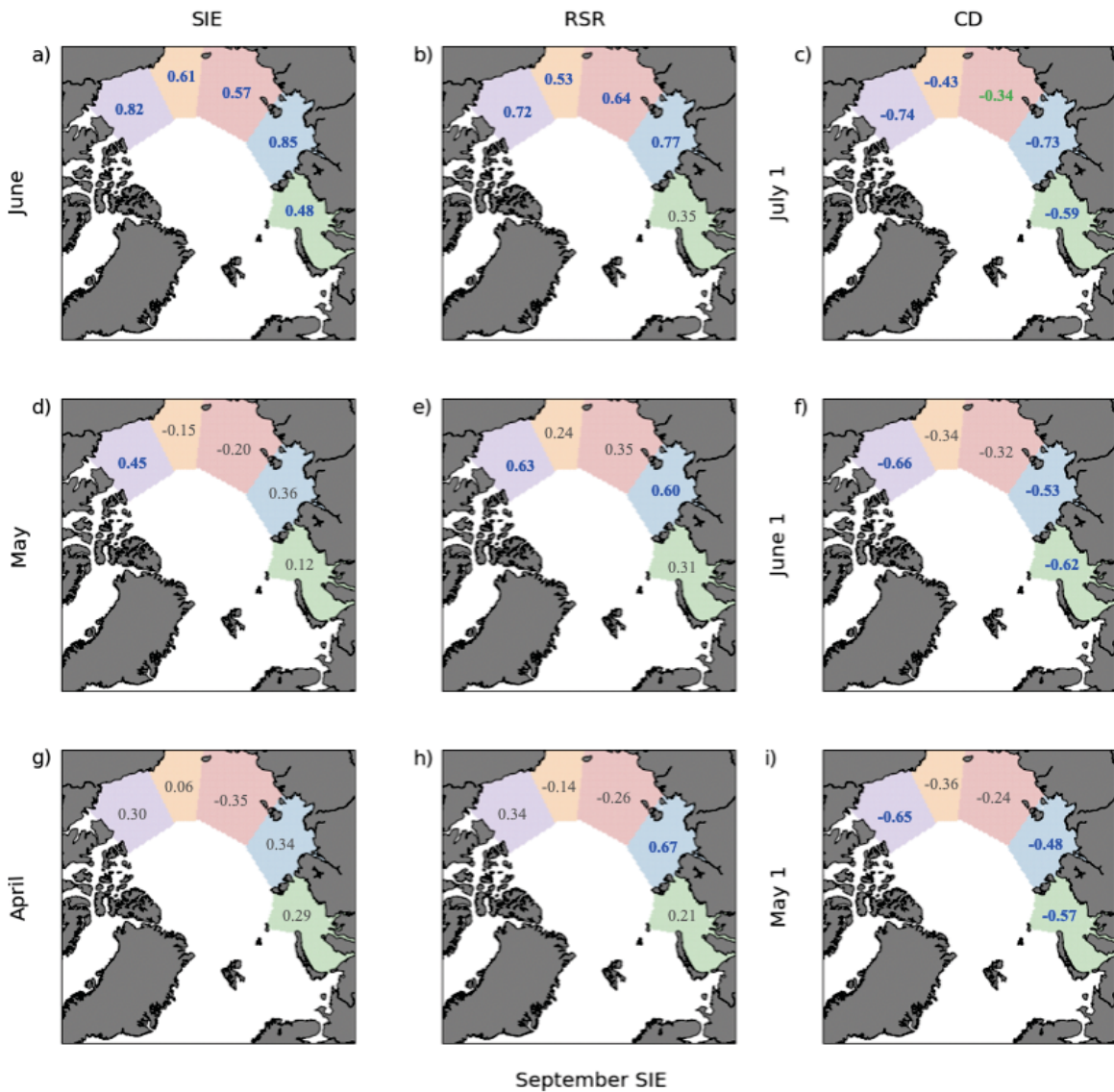
Figure 4.2: Pearson correlation coefficients between detrended June (a-b), May (d-e) and April (g-h) SIE (left column) and all-sky Reflected Solar Radiation (RSR) (middle column) and Coastal Divergence (CD, right column) area anomalies integrated from optimal start week WX (see Table B.1) to c) July 1, f) June 1, i) May 1, and minimum SIE anomalies for each Arctic peripheral sea for the 2000-2018 (SIE and RSR) and 1993-2018 (CD) time period. Correlations significant at the 95 % and 90 % confidence levels and non-significant correlations appear in blue, green and grey, respectively. Correlations using sea ice area instead of SIE are the same (not shown). Correlations between clear-sky RSR and minimum SIE anomalies are the same as for all-sky RSR within uncertainties (see Table A1) except for the Chukchi Sea in June and Laptev Sea in April (not shown). This suggests that atmospheric processes are important for those seas and forecast dates.

19

4.2.1 Beaufort Sea

In the Beaufort Sea, the predictive skill of SIE and RSR is high (r^2 = 0.67; 0.52) and significant for the month of June, medium for the month of May (r^2 = 0.20; 0.40) and low and insignificant for the month of April (r^2 = 0.09; 0.12). CD, however, remains highly correlated (r^2 = 0.54, 0.44, 0.42) for all forecast dates (Figure 4.2). The comparable skill between June RSR and July-1 CD supports the idea that the predictive skill of June RSR comes from sea ice thickness anomalies at the onset of the melt season (Brunette et al., 2019; Bushuk et al., 2017a; Chevallier and Salas-Mélia, 2012; Nikolaeva and Sesterikov, 1970; Williams et al., 2016).

The predictive skill of SIE and RSR in June originates from the presence of open water (Figure 4.1c). In May, SIE and RSR show predictive skill as the open water signal associated with the Amundsen Gulf polynya is strong (Figure 4.1g). The predictive skill is lower, however (Figure 4.2d), despite SIC still explaining 78% of the mean variance in clear-sky RSR in the Beaufort Sea (Figure 4.1c) in areas where SIC variability is greater than 5%. This is because the size of this area is much smaller compared to June. In April, both SIE and RSR lose skill in the Beaufort Sea when the area with SIC variability greater than 5% is nearly zero.

In this sea, while periods of coastal convergence and divergence oscillate throughout winter, spring ice dynamics does give predictability. For instance, a large fraction (55%) of tracers were advected out of the Beaufort Sea between the third week of March (W12) and May 1 in 2008 (not shown), a year with the second lowest minimum in the regional SIE during 1993-2018 (see also Hutchings and Rigor, 2012). Our results are in accord with the findings of Kimura et al. (2013) who observe a steady divergence of sea ice tracers in the Beaufort, Laptev and Kara seas from December 1 to April 30 in 2003-2011 with a similar ice tracking system using daily-ice velocity from the satellite passive microwave sensor Advanced Microwave Scanning Radiometer-Earth Observing System data. Finally, we note that CD remain significantly correlated with the minimum SIE for a June 1 forecast (although with a smaller correlation coefficient r = -0.53) for the entire satellite record

(1979-today), indicating that CD remains a skillful predictor even when years with a thicker and slower ice cover are included.

4.2.2 Chukchi Sea

In the Chukchi Sea, SIE and RSR are equally skillful predictors (within uncertainty, r^2 = 0.37; 0.28) for the month of June and lose all skill for the month of May and April (Figure 4.2). Similarly, CD shows predictive skill for a July 1 forecast but loses skill for June 1 and May 1 forecasts. This suggest that other (summer) processes (e.g. OHT, ice drift) govern the interannual variability in the regional minimum SIE. For instance, Bering Strait OHT in spring is a skillful predictor of SIE in June and July with a resurgence of skill in late Fall (Lenetsky et al., 2020; Serreze et al., 2016; Woodgate et al., 2010), and on the rapid loss of SIE in forced climate simulations (Auclair and Tremblay, 2018). Francis et al. (2005) used an observational data set from TIROS Operational Vertical Sounder (TOVS) for LWD, winds and sensible heat to report that the variance in minimum SIE anomalies in the Chukchi Sea is primarily explained by LWD from June to September ($\approx$ 20-55%), advective heat in the month before the maximum SIE retreat ($\approx$ 10%), and meridional winds early in the melt season ($\approx$ 25%). The fact that CD for a July 1 forecast shows predictive skill (Figure 4.2c) supports the statement of summer dynamics influencing the variability of the regional minimum SIE. A multivariate model using Bering Strait OHT is investigated in Section 4.3.

Finally, clear-sky and all-sky RSR showing equal predictive skill of the minimum SIE (within uncertainty) in all peripheral seas for June except in the Chukchi Sea, where clear-sky RSR shows no skill, suggests that early summer atmospheric radiative fluxes also play a role in this peripheral sea (not shown).

4.2.3 East Siberian Sea

In the East Siberian Sea, SIE and RSR are equally skillful predictors of the minimum SIE in June (r^2 = 0.32; 0.41) and lose all predictive skill in May and April. In May, SIE is no longer a skillful predictor (Figure 4.2d) despite the fact that it is significantly correlated

with clear-sky RSR along the flaw-lead polynya (Figure 4.1g). Flaw-lead polynyas are regions of open water formed between fast ice and pack ice caused by off-shore winds (Bareiss and Görgen, 2005). In this peripheral sea, sea ice motion is mostly parallel to the shore along the circumpolar-flaw lead polynya rather than off-shore (Kwok et al., 2013), and is therefore less likely to create sea ice thickness anomalies over extended areas. We hypothesize that dynamic preconditioning in this region is not associated with surface SIC anomalies, and potentially explains the loss of skill in May SIE.

For a July 1 forecast, CD shows lower (significant at the 90% confidence level) predictive skill for the minimum SIE and no predictive skill for June 1 and May 1 forecasts (Figure 4.2c, f, i). This supports the suggestions above that divergent sea ice motion is small and does not lead to extensive sea ice thickness anomalies (see Appendix B for more discussion). The East Siberian Sea generally shows more convergence of ice from the tracer advection compared to other peripheral seas (not shown) despite some interannual variability. This is consistent with Kwok (2006) and Kimura et al. (2013), who also report convergent winter ice motion in this peripheral sea from a similar satellite-based ice tracking algorithm. A testament to this convergence of sea ice occurred in the winter of 2017 when Russian ice breakers Kapitan Dranitsyn and Admiral Makarov were beset on their way to Arkhangelsk in the East Siberian Sea from thick ridged ice while on a mission to test the Northern Sea Route under a warming Arctic (Staalesen, 2017). As a result, June RSR and SIE are better predictors of the minimum SIE in this peripheral sea.

While there is little off-shore ice motion in late winter, Francis et al. (2005) reports on LWD anomalies explaining the majority of variance in the minimum SIE anomalies in the month before the maximum SIE retreat ($\approx 35\%$), with southerly wind anomalies also having some influence at the time of maximum retreat ($\approx 10\%$) through sea ice advection that enhances thermodynamic anomalies (Rigor et al., 2002).

4.2.4   Laptev Sea

In the Laptev Sea, SIE and RSR again show equal predictive skill for June (r^2 = 0.72; 0.59); however, SIE loses predictive skill for May and April while RSR remains skillful (Figure 4.2d-e, g-h). This is despite May SIC still explaining 61% of mean variance in clear-sky RSR where correlation is significant and SIC variability is greater than 5% (Figure 4.1g). However, the areal extent where SIC variability is greater than 5% is much smaller compared to June. The fact that clear-sky RSR has equal predictive skill of the minimum SIE as all-sky RSR (not shown) suggests that the atmosphere is not responsible for this difference, leaving MPF and/or SIT anomalies as the potential source of May predictive skill in the Laptev Sea.

This statement is supported by the significant correlation found between May RSR and June-1 CD in the Laptev Sea (not shown). In other words, RSR reflects the surface albedo variation that is a function of sea ice thickness anomalies (Light et al., 2015) preconditioned from CD. This argument of SIT anomalies at the surface, in addition to SIC and MPF, explaining the variance in all-sky RSR is corroborated by the following: the variance in clear-sky RSR explained by each surface component – SIC and MPF (Figure 4.1g, h) – does not sum up to the variance in all-sky RSR explained by the total surface – clear-sky RSR (Figure 4.1e), i.e. another surface component is responsible.

A less convincing argument for the potential source of May predictive skill is MPF, where clear-sky MPF and clear-sky RSR correlations are only significant in very localized regions in this peripheral sea (r = -0.75, see Figure 4.1h). However, the unconvincing results could also potentially be from the uncertainties and the shorter period that come with the MPF data, rather than from an actual lack in skill.

In April, clear-sky RSR explains a smaller fraction of the variance in all-sky RSR (68%) than that in June (88%) and May (85%), indicating an increased contribution from the atmosphere. Moreover, clear-sky RSR shows lower predictive skill of the minimum SIE at a 90% confidence level than all-sky RSR, further supporting the idea that atmospheric radiative fluxes play a role (not shown).

The increased surface air temperature associated with the ubiquitous presence of polynya in the Laptev Sea compared with other peripheral seas (Barber and Massom, 2007; Bareiss and Görgen, 2005) may explain why RSR remains skillful in contrast with SIE (see Figure 4.1g and k for polynya signatures). A flaw-lead polynya of approximately 2000 km in length with width between 10-100 km (Morales Maqueda et al., 2004) is present in the Laptev Sea from November until April along the fast ice edge in the southern latitudes (Willmes et al., 2011) where shortwave radiation can reach even at high solar zenith angles before summer solstice. In the winter, approximately 50% of ocean-atmosphere heat loss occurs over polynyas and leads (Maykut, 1982). By late April, the net ocean-atmosphere heat flux (including shortwave radiation) can instead cause surface heat gain (Willmes et al., 2011), increasing water vapor content in the atmosphere and clouds (Bareiss and Görgen, 2005). While surface albedo increases dramatically with increasing solar zenith angle under clear-sky conditions, the presence of clouds increases diffuse radiation that leads to a lower surface albedo (Gardner and Sharp, 2010; Hartmann, 2016). Choi et al. (2014) also attribute the positive correlation found between cloud fraction and absorbed solar radiation in April and May to this cloud effect at higher solar zenith angles.

CD is a skillful predictor in the Laptev Sea for all forecast dates. This peripheral sea shows ubiquitous off-shore ice motion throughout winter and the highest percentage of tracers lost due to coastal divergence (and melt for July 1 forecasts) for all forecast dates (not shown). Our results are in accord with the findings of Brunette et al. (2019) who find predictive skill in the Laptev Sea for a May 1 forecast and Kimura et al. (2013) who show a steady divergence of sea ice tracers in the same sea integrated from December 1 to April 30.

4.2.5 Kara Sea

In the Kara Sea, SIE is a skillful predictor of the minimum SIE only for June ($r^2 = 0.23$) unlike RSR that has no skill for any forecast date (Figure 4.2). This is in agreement with Choi et al. (2014) who report an absence of significant covariance between early

summer TOA solar radiation and late summer SIC in the Kara Sea. Two factors can be responsible for the difference in correlation between June RSR and SIE: the presence of clouds in regions of large open water or the presence of an extensive ponded ice cover. The fact that MPF is positively correlated with clear-sky RSR in the Kara Sea (Figure 4.1d) suggests that clouds over open water is responsible for the lack of predictive skill in June RSR. Furthermore, clouds have a large impact on the planetary albedo in regions with low SIC as in the Kara Sea (Choi et al., 2019; Gorodetskaya et al., 2006). However, the reduced ice-albedo feedback associated with summer clouds does not have a large effect on the minimum SIE in this sea where it is currently almost a seasonal ice cover with low SIC already by June. The results are also in agreement with Zhan and Davies (2017) who report that June RSR's predictability is mainly attributed to surface albedo anomalies rather than atmospheric conditions such as clouds, water vapor, aerosol and surface air temperature. We conclude that clouds and uncertainties in MPF explain the lack of correlation in June RSR.

For May and April, both SIE and RSR lose skill. This is despite the significant and negative correlation found between May MPF and clear-sky RSR in this sea (r = -0.74). As discussed in Section 4.1, this is presumably due to open water anomalies outweighing the effects of melt pond in creating negative anomalies of the minimum SIE. In April, predictive skill is lost due to lack of surface albedo anomalies.

CD is a skillful predictor of the minimum SIE for all forecast dates. As mentioned for the Laptev Sea, the Kara Sea also shows consistent coastal divergence and the highest percentage of tracers lost due to divergence (and melt for July 1 forecasts) for all forecast dates (not shown), in line with the steady divergence of sea ice tracers reported by Kimura et al. (2013). This confirms the hypothesis that open water anomalies created by offshore advection of sea ice dominates the predictability in this sea.

In summary, RSR and SIE have equal predictive skill in all peripheral seas (except in the Kara Sea) for a July 1 forecast and their predictive skill is mainly due to open water at the surface. For a June 1 forecast, RSR is a more skillful predictor than SIE in the Laptev Sea, where SIE loses predictive skill, as RSR appears to reflect ice thickness anomalies through surface albedo. For a May 1 forecast (i.e. before melt onset), RSR

and SIE are both non-skillful predictors of the minimum SIE in the peripheral seas. One exception is the Laptev Sea where RSR shows significant skill, most likely from coastal polynyas and associated atmospheric effects. Overall, for most peripheral seas, RSR and SIE's predictive skill that relies on summer thermodynamics is capped at a lead-time of 3 months (July 1 forecast) and CD remains skillful at a longer lead-time for the Beaufort, Laptev and Kara seas.

4.3 Hindcast Model

We develop three hindcast models M1, M2 and M3 for the minimum SIE for 2000-2018 in each peripheral sea based on the linear trend (M1), linear trend + CD integrated from start week WX (see Table B.1) to May 1 (M2) and linear trend + April RSR (M3). The 2000-2018 period is selected based on availability of RSR data. The simplest model (M1) is written mathematically as $SIE_p = a\,t + C$, where SIE_p is the predictand, t is time (year) and C is a constant. M2 is based on the linear trend and May-1 CD (X_1) as predictors: $SIE_p = a\,t_1 + b\,X_1 + C$. M3 is based on the linear trend and April RSR (X_2) as predictors: $SIE_p = a\,t + c\,X_2 + C$. All constants (a, b and c) are determined from the method of least-squares. We use the adjusted coefficient of determination ($\bar{r}^2$) to take into account the fact that increasing the number of predictors in a statistical model increases the correlation even if the new predictor is not correlated with the predictand.

The linear trend in M1 explains 29%, 30%, 15%, 32% and 47 % of the variance in the minimum SIE ($\bar{r}^2$) in the Beaufort, Chukchi, East Siberian, Laptev and Kara Seas, respectively (Table 4.1). In general, the fraction of variance explained by the linear trend is related to the relative magnitude of the interannual variability in the minimum SIE compared to the trend (Figure 4.3). For instance, the linear trend explains the smallest fraction of the variance in the East Siberian Sea where the interannual variability is large and explains the largest fraction of the variance in the Kara Sea where the interannual variability is small and the trend is large (see Figure 4.3). The large interannual variability in the East Siberian Sea shows that winter (strong convergence event related to persistence

26

Table 4.1: Correlation coefficients (r^2), adjusted correlation coefficients ($\bar{r}^2$) and standard deviation of hindcast error (σ_{err}) in millions km^2 for hindcast models of the September SIE from 2000 to 2018 for each peripheral sea using linear trend (M1), linear trend and May-1 Coastal Divergence (CD) area anomalies (M2) and linear trend and April RSR anomalies (M3). Bold characters indicate significant improvement in predictability using an additional predictand.

	Model	Predictors	r^2	$\bar{r}^2$	σ_{err}
Beaufort	M1	Linear Trend	0.33	0.29	0.15
	M2	Linear Trend, May-1 CD	0.51	**0.45**	0.13
	M3	Linear Trend, April RSR	0.41	0.33	0.15
Chukchi	M1	Linear Trend	0.34	0.30	0.11
	M2	Linear Trend, May-1 CD	0.49	**0.43**	0.10
	M3	Linear Trend, April RSR	0.35	0.27	0.11
East Siberian	M1	Linear Trend	0.19	0.15	0.24
	M2	Linear Trend, May-1 CD	0.20	0.10	0.24
	M3	Linear Trend, April RSR	0.25	0.15	0.24
Laptev	M1	Linear Trend	0.36	0.32	0.15
	M2	Linear Trend, May-1 CD	0.51	**0.45**	0.13
	M3	Linear Trend, April RSR	0.65	**0.61**	0.11
Kara	M1	Linear Trend	0.50	0.47	0.09
	M2	Linear Trend, May-1 CD	0.62	**0.58**	0.08
	M3	Linear Trend, April RSR	0.52	0.46	0.09

of ice thickness anomalies) and summer mechanisms explain the rest of the variance in minimum SIE.

The M2 hindcast model (linear trend + May-1 CD) increases the adjusted coefficient of determination ($\bar{r}^2$) and decreases the hindcast error (σ_{err}) for all seas except for the East Siberian Sea (Table 4.1). Specifically, $\bar{r}^2$ increases by 16% (0.29 to 0.45), 13% (0.30 to 0.43), 13% (0.32 to 0.45) and 11% (0.47 to 0.58) for the Beaufort, Chukchi, Laptev and Kara Seas, respectively, and the hindcast error decreases by 10 to 20 thousand km^2, or
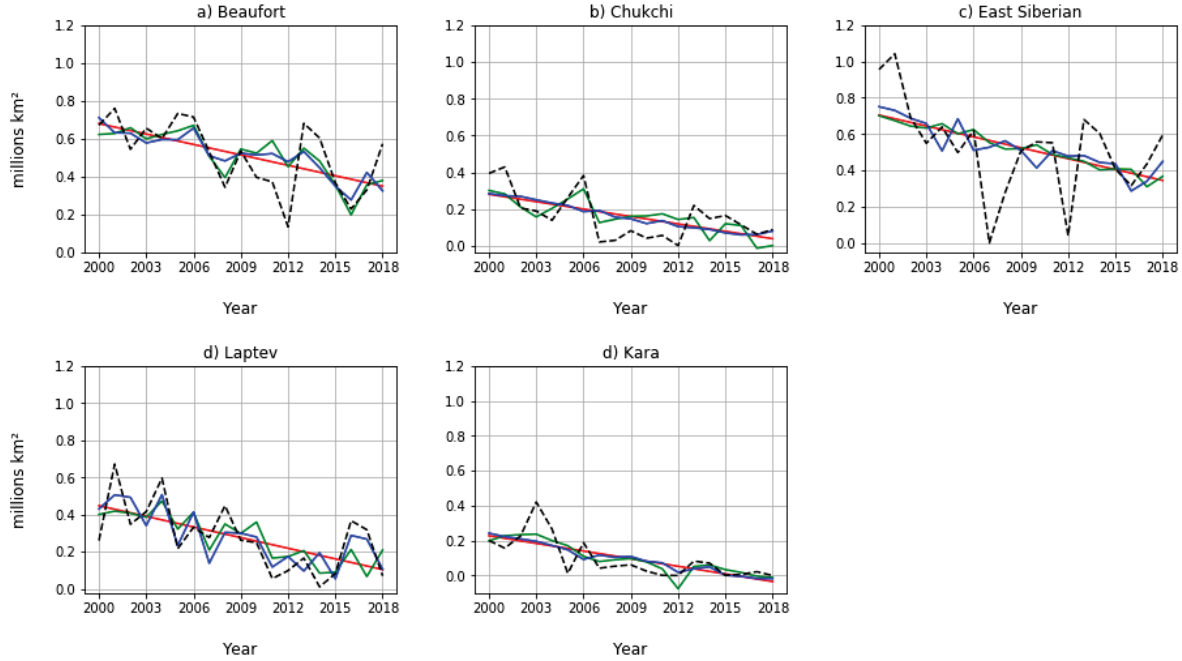
Figure 4.3: Hindcasts of SIE observations (black dashed line) from M1 (linear trend, red), M2 (linear trend and May-1 Coastal Divergence (CD) anomalies, green) and M3 (linear trend and April RSR anomalies, blue) for each peripheral sea.

approximately 1–2% of each peripheral sea area. The largest improvement for the M2 model is in the Beaufort Sea ($\bar{r}^2_{M1} = 0.29$ to $\bar{r}^2_{M2} = 0.45$). This result is counter-intuitive as the largest predictive skill for the minimum SIE from CD was expected to come from the Laptev Sea where offshore ice motion is ubiquitous in late winter (Brunette et al., 2019; Nikolaeva and Sesterikov, 1970; Rigor et al., 2002; Williams et al., 2016). The 13% increase in the Laptev Sea is slightly lower than that reported by Brunette et al. (2019) who used a slightly different time period and a larger Laptev Sea domain.

For the East Siberian Sea, the interannual variability of the minimum SIE is small relative to that in 2007 and 2012 when two all-time record low minimum SIE occurred (black dashed line in Figure 4.3c). The Beaufort and Chukchi seas also show large negative SIE anomalies for those two record minimum years (black dashed line in Figure 4.3a, b), however, those anomalies are not significantly larger than the general interannual variability in these peripheral seas. Hence, the loss of ice in the East Siberian Sea was the main contributor to the record low SIE in those years. In summer 2007, a semi-permanent high over the Beaufort Sea and a strong positive dipole anomaly

(Wang et al., 2009) led to sustained winds exporting sea ice out of the Arctic and large solar radiation anomalies in the largely ice-free Beaufort Sea with summer sea surface temperature anomalies reaching up to 5°C (Steele et al., 2008). In August 2012, an extreme storm that formed over the East Siberian Sea led to surface divergence and facilitated summer melt (Parkinson and Comiso, 2013; Simmonds and Rudeva, 2018).

Hindcast model M3 (linear trend + April RSR) does not improve the May 1 forecast skill compared to that based on only the linear trend (M1), except for the Laptev Sea (see Table 4.1). The Laptev Sea experiences a significant increase from M1 to M3 by 29% ($\bar{r}^2_{M1}$ = 0.32 to $\bar{r}^2_{M3}$ = 0.61) and is also higher than that of M2 ($\bar{r}^2_{M2}$ = 0.45).

Finally, we find that $\bar{r}^2$ from a hindcast model based on linear trend and June RSR (Beaufort: 0.64, Chukchi: 0.47, East Siberian: 0.47, Laptev: 0.71, Kara: 0.50) are comparable (within 10%) to a hindcast model based on linear trend and June SIE (Beaufort: 0.75, Chukchi: 0.53, East Siberian: 0.37, Laptev: 0.80, Kara: 0.56) for all peripheral seas. This supports the hypothesis that June RSR anomalies largely stem from June SIC anomalies preconditioned in late winter. We also confirm that adding Bering Strait April OHT to M2 and April–May OHT to linear trend + June-1 CD do not improve $\bar{r}^2$ for neither the Chukchi Sea nor the East Siberian Sea (not shown). This is in accord with Lenetsky et al. (2020) who find that April–May OHT significantly correlates with June and July SIE in the Chukchi Sea, but loses significance with August and September SIE. The loss of significance after July is attributed to summer dynamical processes and the sea ice edge retreating northward over the deep Canadian Basin where ocean heat flux and sea ice interaction is reduced.

Chapter 5

Conclusion

5.1 Conclusion

This study compares a regional seasonal sea ice forecasting model of the minimum Sea Ice Extent (SIE) using satellite-derived Reflected Solar Radiation (RSR) and SIE and show that Coastal Divergence (CD) explains most of the predictive skill in RSR and SIE. The key conclusions are as follows:

- The predictive skill of RSR mainly arises from open water anomalies and is essentially equivalent to SIE.

- In June, Melt Pond Fraction (MPF) is negatively correlated with RSR in the central Arctic; however, it is positively correlated (counter-intuitively) in the peripheral seas. This is because large MPF in June in the peripheral seas implies "presence of sea ice" at the surface and low MPF implies absence of sea ice or open water. We find that June RSR has predictive skill in all the peripheral seas since the signal from "presence of ponded sea ice" is smaller than the signal from open water.

- RSR and SIE are equally good predictors for all peripheral seas for a July 1 forecast, only for the Beaufort Sea for a June 1 forecast and has no predictive skill for a May 1 forecast. There are two exceptions: the Kara Sea where only SIE has predictive skill for a July 1 forecast and the Laptev Sea where only RSR has predictive skill

for June 1 and May 1 forecasts. We hypothesize that clouds, melt ponds and underlying sea ice introduces uncertainties in RSR for the Kara Sea. For the Laptev Sea, SIE lacks predictability as it does not reflect the albedo variability from ice thickness anomalies in May and atmospheric contribution from high concentration of polynyas in April that give RSR the predictive skill.

- CD has equal predictive skill compared to RSR for all peripheral seas for a July 1 forecast. For longer lead-times, CD and RSR both lose skill in the East Siberian and Chukchi seas. In the Beaufort Sea, only CD remains skillful for all forecast lead-times.

- The predictive skill in the East Siberian and the Chukchi seas is dominated by summer processes. The Kara Sea is an outlier in this simple model, where CD remains always skillful for all forecast dates while RSR never shows skill. This is because sea ice thickness and SIC anomalies that give predictive skill are absent in RSR in the Kara Sea due to uncertainties introduced from clouds and melt ponds.

- A simple hindcast model for 2000-2018 using the linear trend (M1) explains 15, 29, 30, 32 and 47% of the variance in the minimum SIE ($\bar{r}^2$) in the East Siberian, Beaufort, Chukchi, Laptev and Kara seas, respectively. The largest explained variability in the Kara Sea highlights the strong trend towards a seasonal ice cover. The lowest explained variance in the East Siberian Sea show that other winter, spring and summer processes explain the rest of the variance to varying degrees.

- The largest improvement in predictive skill from adding May-1 CD to the linear trend was surprisingly found in the Beaufort Sea ($\bar{r}^2_{M1} = 0.29$ to $\bar{r}^2_{M2} = 0.45$ and $\sigma_{err\ M1} = 0.15$ to $\sigma_{err\ M2} = 0.13$). This is believed to be from the semi-permanent off-shore motion of ice, reduced sea ice thickness and increased mobility in recent years. May-1 CD adds skill to the forecast in the Laptev Sea ($\bar{r}^2_{M1} = 0.32$ to $\bar{r}^2_{M2} = 0.45$ and $\sigma_{err\ M1} = 0.15$ to $\sigma_{err\ M2} = 0.13$), slightly less than the 21% reported by Brunette et al. (2019). May-1 CD adds predictive skill in the Kara Sea ($\bar{r}^2_{M1} = 0.47$ to $\bar{r}^2_{M2} = 0.58$ and $\sigma_{err\ M1} = 0.09$ to $\sigma_{err\ M2} = 0.08$), however, the implication of the predictability

in this sea is minor due to its fast transition to a seasonal ice cover. In fact, the predictive skill ($\bar{r}^2{}_{M2}$) is better for the time period of 1993-2018 than 2000-2018 when summer SIE in this sea was greater.

- Besides the Laptev Sea (where April RSR shows higher skill than May-1 CD) and the East Siberian Sea (where neither May-1 CD and April RSR show skill), May-1 CD has better predictive skill than April RSR for the same lead-time in all peripheral seas.

- Bering Strait OHT does not improve forecast skill in neither the Chukchi Sea nor the East Siberian Sea. In the two peripheral seas, the ocean-sea ice interaction with the OHT is lost further into the summer as the SIE retreats further north with summer melt and advection.

Our study identified key dynamic and thermodynamic mechanisms that govern the minimum SIE for each Arctic peripheral sea. CD is skillful for May 1 and June 1 seasonal forecasts in the Beaufort, Laptev and Kara seas. Future work includes identifying sources of correlation between LWD, CD and the minimum SIE. This is based on the hypothesis that LWD and CD may be correlated with a tertiary variable (i.e. large-scale atmospheric circulation) that affect the minimum SIE.

Bibliography

Auclair, G., and L. B. Tremblay, 2018: The Role of Ocean Heat Transport in Rapid Sea Ice Declines in the Community Earth System Model Large Ensemble. *J. Geophys. Res. Oceans*, **123 (12)**, 8941–8957, doi:https://doi.org/10.1029/2018JC014525.

Babb, D. G., J. Landy, D. Barber, and R. Galley, 2019: Winter sea ice export from the Beaufort Sea as a preconditioning mechanism for enhanced summer melt: A case study of 2016. *J. Geophys. Res. Oceans*, **124**, 6575–6600, doi:https://doi.org/10.1029/2019JC015053.

Barber, D., and R. Massom, 2007: Chapter 1 The Role of Sea Ice in Arctic and Antarctic Polynyas. *Polynyas: Windows to the World*, W. Smith, and D. Barber, Eds., Elsevier Oceanography Series, Vol. 74, Elsevier, 1–54, doi:https://doi.org/10.1016/S0422-9894(06)74001-6.

Bareiss, J., and K. Görgen, 2005: Spatial and temporal variability of sea ice in the Laptev Sea: Analyses and review of satellite passive-microwave data and model results, 1979 to 2002. *Global Planet. Change*, **48 (1)**, 28 – 54, doi:10.1016/j.gloplacha.2004.12.004.

Blanchard-Wrigglesworth, E., K. C. Armour, C. M. Bitz, and E. Deweaver, 2011: Persistence and inherent predictability of Arctic sea ice in a GCM ensemble and observations. *J. Clim.*, **24 (1)**, 231–250, doi:10.1175/2010JCLI3775.1.

Brunette, C., B. Tremblay, and R. Newton, 2019: Winter Coastal Divergence as a Predictor for the Minimum Sea Ice Extent in the Laptev Sea. *J. Clim.*, **32**, 1063–1080, doi:https://doi.org/10.1175/JCLI-D-18-0169.1.

Bushuk, M., R. Msadek, M. Winton, G. A. Vecchi, R. Gudgel, A. Rosati, and X. Yang, 2017a: Summer Enhancement of Arctic Sea Ice Volume Anomalies in the September-Ice Zone. *J.Clim.*, **30**, 2341–2362, doi:10.1175/JCLI-D-16-0470.1.

Bushuk, M., R. Msadek, M. Winton, G. A. Vecchi, R. Gudgel, A. Rosati, and X. Yang, 2017b: Skillful regional prediction of Arctic sea ice on seasonal timescales. *Geophys. Res. Lett.*, **44**, 4953–4964, doi:10.1002/2017GL073155.

Bushuk, M., M. Winton, D. B. Bonan, E. Blanchard-Wrigglesworth, and T. Delworth, 2020: A mechanism for the Arctic sea ice spring predictability barrier. *Geophys. Res. Lett.*, **47**, e2020GL088 335, doi:10.1029/2020GL088335.

Cao, Y., S. Liang, X. Chen, T. He, D. Wang, and X. Cheng, 2017: Enhanced wintertime greenhouse effect reinforcing Arctic amplification and initial sea-ice melting. *Sci.Rep.*, **7**, 8462, doi:https://doi.org/10.1038/s41598-017-08545-2.

CERES Science Team, 2018: *CERES EBAF Ed 4.0 Data Quality Summary*. Available at https://ceres.larc.nasa.gov/documents/DQ summaries/CERES EBAF Ed4.0 DQS.pdf.

CERES Science Team, 2020: *CERES EBAF Surface Ed 4.1 Data Quality Summary*. Available at https://ceres.larc.nasa.gov/documents/DQ summaries/CERES EBAF-Surface Ed4.1 DQS.pdf.

Chevallier, M., and D. Salas-Mélia, 2012: The role of the sea ice thickness distribution in the Arctic sea ice potential predictability: A diagnostic approach with a coupled GCM. *J. Clim.*, **25**, 3025–3038, doi:10.1175/JCLI-D-11-00209.1.

Choi, Y., J. Hwang, J. Ok, D. S. R. Park, H. Su, J. H. Jiang, L. Huang, and T. Limpasuvan, 2019: Effect of Arctic clouds on the ice-albedo feedback in midsummer. *International Journal of Climatology*, **20**, doi:10.1002/joc.6469.

Choi, Y. S., B. M. Kim, S. K. Hur, S. J. Kim, J. H. Kim, and C. H. Ho, 2014: Connecting early summer cloud-controlled sunlight and late summer sea ice in the Arctic. *J. Geophys. Res. Atmos.*, **119**, 11, 087–11, 099, doi:10.1002/2014JD022013.

Comiso, J. C., 2012: Large Decadal Decline of the Arctic Multiyear Ice Cover. *J. Clim.*, **25**, 1176–1193, doi:10.1175/JCLI-D-11-00113.1.

DeRepentigny, P., B. Tremblay, R. Newton, and S. Pfirman, 2016: Patterns of sea ice retreat in the transition to a seasonally icefree Arctic. *J. Clim.*, **29**, 6993–7008, doi:https://doi.org/10.1175/JCLI-D-15-0733.1.

Emery, W. J., C. Fowler, and J. Maslanik, 1995: *Satellite remote sensing of ice motion, in Oceanographic Applications of Remote Sensing*. ed. Motoyoshi Ikeda and Frederic W. Dobson. CRC Press, Boca Raton, FL.

Francis, J. A., E. Hunter, J. Key, and X. Wang, 2005: Clues to variability in Arctic minimum sea ice extent. *Geophys. Res. Lett.*, **32**, L21 501, doi:10.1029/2005GL024376.

Gardner, A. S., and M. J. Sharp, 2010: A review of snow and ice albedo and the development of a new physically based broadband albedo parameterization. *J. Geophys. Res.*, **115**, F01 009, doi:10.1029/2009JF001444.

Gorodetskaya, I., L. B. T. M. A. Cane, and A. Kaplan, 2006: The effects of sea-ice and land-snow concentrations on planetary albedo from the earth radiation budget experiment. *Atmos. Ocean*, **44**, 195–205, doi:10.3137/ao.440206.

Guemas, V., M. Chevallier, M. Déqué, O. Bellprat, and F. Doblas-Reyes, 2016: Impact of sea ice initialization on sea ice and atmosphere prediction skill on seasonal timescales. *Geophys. Res. Lett.*, **43**, 3889–3896, doi:10.1002/2015GL066626.

Hartmann, D. L., 2016: Chapter 10 - Climate Sensitivity and Feedback Mechanisms. *Global Physical Climatology*, D. L. Hartmann, Ed., Second ed., Elsevier, Boston, 293 – 323, doi:https://doi.org/10.1016/B978-0-12-328531-7.00010-4, URL http://www.sciencedirect.com/science/article/pii/B9780123285317000104.

Holland, M. M., D. A. Bailey, and S. Vavrus, 2011: Inherent sea ice predictability in the rapidly changing Arctic environment of the Community Climate System Model, version 3. *Climate Dyn.*, **36**, 1239–1253, doi:10.1007/s00382-010-0792-4.

Huang, Y., G. Chou, Y. Xie, and N. Soulard, 2019: Radiative control of the interannual variability of Arctic sea ice. *Geophys. Res. Lett.*, **46 (16)**, 9899–9908, doi:10.1029/2019GL084204.

Hutchings, J. K., and I. G. Rigor, 2012: Role of ice dynamics in anomalous ice conditions in the Beaufort Sea during 2006 and 2007. *J. Geophys. Res. Oceans*, **117**, C00e04(C8), doi:10.1029/2011jc007182.

Kapsch, M., R. Graversen, M. Tjernström, and R. Bintanja, 2016: The Effect of Downwelling Longwave and Shortwave Radiation on Arctic Summer Sea Ice. *J. Clim.*, **29**, 1143–1159, doi:10.1175/JCLI-D-15-0238.1.

Kashiwase, H., K. I. Ohshima, S. Nihashi, and H. Eicken, 2017: Evidence for ice-ocean albedo feedback in the Arctic Ocean shifting to a seasonal ice zone. *Sci. Rep.*, **31**, 8170, doi:10.1038/s41598-017-08467-z.

Kato, S., and Coauthors, 2018: Surface Irradiances of Edition 4.0 Clouds and the Earth's Radiant Energy System (CERES) Energy Balanced and Filled (EBAF) Data Product. *J. Clim.*, **31**, 4501–4527, doi:10.1175/JCLI-D-17-0523.1.

Kimura, N., A. Nishimura, Y. Tanaka, and H. Yamaguchi, 2013: Influence of winter sea-ice motion on summer ice cover in the Arctic. *Polar Research*, **32**, doi:10.3402/polar.v32i0.20193.

Krumpen, T., M. Janout, K. I. Hodges, R. Gerdes, F. Girard-Ardhuin, J. A. Höleman, and S. Willmes, 2013: Variability and trends in Laptev sea ice outflow between 1992-2011. *The Cryosphere*, **7 (1)**, 349–363, doi:10.5194/tc-7-349-2013.

Kwok, R., 2006: Contrasts in sea ice deformation and production in the Arctic seasonal and perennial ice zones. *J. Geophys. Res.*, **111**, C11S22, doi:10.1029/2005JC003246.

Kwok, R., 2018: Arctic sea ice thickness, volume, and multiyear ice coverage: losses and coupled variability (1958–2018). *Environ. Res. Lett.*, **13**, 105 005, doi:10.1088/1748-9326/aae3ec.

Kwok, R., G. F. Cunningham, and S. V. Nghiem, 2003: A study of the onset of melt over the Arctic Ocean in RADARSAT synthetic aperture radar data. *J. Geophys. Res.*, **108 (C11)**, 3363, doi:10.1029/2002JC001363.

Kwok, R., G. Spreen, and S. Pang, 2013: Arctic sea ice circulation and drift speed: Decadal trends and ocean currents. *J. Geophys. Res. Oceans*, 2408–2425, doi:10.1002/jgrc.20191.

Lenetsky, J., B. Tremblay, and C. Brunette, 2020: Sub-Seasonal predictability of Arctic Ocean sea ice conditions: Bering strait and Ekman-driven Ocean Heat Transport. *Manuscript submitted for publication*.

Letterly, A., J. Key, and Y. Liu, 2016: The influence of winter cloud on summer sea ice in the Arctic. *J. Geophys. Res. Atmos.*, **121**, 2178–2187, doi:10.1002/2015JD024316.

Light, B., D. K. Perovich, M. A. Webster, C. Polashenski, and R. Dadic, 2015: Optical properties of melting first-year Arctic sea ice. *J. Geophys. Res. Oceans*, **120**, 7657– 7675, doi:10.1002/2015JC011163.

Lindsay, R. W., J. Zhang, A. J. Schweiger, and M. A. Steele, 2008: Seasonal predictions of ice extent in the Arctic Ocean. *J. Geophys. Res.*, **113**, C02 023, doi:10.1029/2007JC004259.

Liu, J., M. Song, R. M. Horton, and Y. Hu, 2015: Revisiting the potential of melt pond fraction as a predictor for the seasonal Arctic sea ice extent minimum. *Environ. Res. Lett.*, **10**, 054 017, doi:10.1088/1748-9326/10/5/054017.

Liu, Y., and J. R. Key, 2014: Less winter cloud aids summer 2013 Arctic sea ice return from 2012 minimum. *Environ. Res. Lett.*, **9**, 044 002, doi:https://doi.org/10.1088/1748-9326/9/4/044002.

Loeb, N. G., B. A. Wielicki, D. R. Doelling, G. L. Smith, D. F. Keyes, S. Kato, N. Manalo-Smith, and T. Wong, 2009: Toward optimal closure of the Earth's top-of-atmosphere radiation budget. *J. Clim.*, **22**, 748–766, doi:10.1175/2008JCLI2637.1.

Loeb, N. G., and Coauthors, 2018: Clouds and the Earth's Radiant Energy System (CERES) Energy Balanced and Filled (EBAF) Top-of-Atmosphere (TOA) Edition 4.0 Data Product. *J. Clim.*, **31 (2)**, 895–918, doi:10.1175/JCLI-D-17-0208.1.

Loeb, N. G., and Coauthors, 2020: Toward a consistent definition between satellite and model clear-sky radiative fluxes. *J. Clim.*, **33**, 61–75, doi:https://doi.org/10.1175/JCLI-D-19-0381.1.

Maslanik, J., J. Stroeve, C. Fowler, and W. Emery, 2011: Distribution and trends in Arctic sea ice age through spring 2011. *Geophys. Res. Lett.*, **38**, L13 502, doi:10.1029/2011GL047735.

Maslanik, J. A., C. Fowler, J. Stroeve, S. Drobot, J. Zwally, D. Yi, and W. Emery, 2007: A younger, thinner Arctic ice cover: Increased potential for rapid, extensive sea-ice loss. *Geophys. Res. Lett.*, **34**, L24 501, doi:10.1029/2007GL032043.

Maykut, G. A., 1982: Large-scale heat exchange and ice production in the central Arctic. *J. Geophys. Res.*, **87 (C10)**, 7971–7984, doi:10.1029/JC087iC10p07971.

Meier, W. N., F. Fetterer, M. Savoie, S. Mallory, R. Duerr, and J. Stroeve, 2017: NOAA/NSIDC Climate data record of passive microwave sea ice concentration, Version 3. [Daily SIC]. *NSIDC: National Snow and Ice Data Center*, doi:https://doi.org/10.7265/N59P2ZTG.[May,2019].

Meier, W. N., M. Savoie, and S. Mallory, 2011, updated 2017: CDR climate algorithm and theoretical basis document: Sea Ice Concentration, Rev 6. ed. F. Fetterer and A. Windnagel. *NOAA NCDC CDR Program*.

Miles, M. W., and R. G. Barry, 1998: A 5-year satellite climatology of winter sea ice leads in the western Arctic. *J. Geophys. Res.*, **103 (C10)**, 21 723– 21 734, doi:10.1029/98JC01997.

Morales Maqueda, M. A., A. J. Willmott, and N. R. T. Biggs, 2004: Polynya dynamics: a review of observations and modeling. *Reviews of Geophysics*, **42**, 1, doi:10.1029/2002RG000116.

Msadek, R., G. A. Vecchi, M. Winton, and R. G. Gudgel, 2014: Importance of initial conditions in seasonal predictions of Arctic sea ice extent. *Geophys. Res. Lett.*, **41**, 5208–5215, doi:10.1002/2014GL060799.

Nikolaeva, A. J., and N. P. Sesterikov, 1970: *A method of calculation of ice conditions (on the example of the Laptev Sea). Ice Forecasting Techniques for the Arctic Seas*. B. A. Krutskih, Z. M. Gudkovic, and A. L. Sokolov, Eds., Amerind Publishing, Boca Raton, FL, 150–230 pp.

Onarheim, I., T. Eldevik, L. Smedsrud, and J. Stroeve, 2018: Seasonal and Regional Manifestation of Arctic sea ice loss. *J. Clim.*, **31**, 4917–4932, doi:https://doi.org/10.1175/JCLI-D-17-0427.1.

Parkinson, C. L., and J. C. Comiso, 2013: On the 2012 record low Arctic sea ice cover: Combined impact of preconditioning and an August storm. *Geophys. Res. Lett.*, **40**, 1356–1361, doi:10.1002/grl.50349.

Peng, G., W. N. Meier, D. Scott, and M. Savoie, 2013: A long-term and reproducible passive microwave sea ice concentration data record for climate studies and monitoring. *Earth System Science Data*, **5 (2)**, 311–318, doi:10.5194/essd-5-311-2013, URL https://www.earth-syst-sci-data.net/5/311/2013/.

Perovich, D. K., and C. Polashenski, 2012: Albedo evolution of seasonal Arctic sea ice. *Geophys. Res. Lett.*, **39**, L08 501, doi:10.1029/2012GL051432.

Perovich, D. K., J. A. Richter-Menge, K. F. Jones, and B. Light, 2008: Sunlight, water, and ice: Extreme Arctic sea ice melt during the summer of 2007. *Geophys. Res. Lett.*, **35**, L11 501, doi:10.1029/2008GL034007.

Preußer, A., K. I. Ohshima, K. Iwamoto, S. Willmes, and G. Heinemann, 2019: Retrieval of Wintertime Sea Ice Production in Arctic Polynyas Using Thermal Infrared and Passive Microwave Remote Sensing Data. *J. Geophys. Res. Oceans*, **124 (8)**, 5503–5528, doi:10.1029/2019JC014976.

Rigor, I. G., and J. M. Wallace, 2004: Variations in the age of Arctic sea-ice and summer sea-ice extent. *Geophys. Res. Lett.*, **31**, L09 401, doi:10.1029/2004GL019492.

Rigor, I. G., J. M. Wallace, and R. L. Colony, 2002: Response of sea ice to the Arctic Oscillation. *J. Clim.*, **15**, 2648–2663, doi:10.1175/1520-0442(2002)015⟨2648:ROSITT⟩2.0. CO;2.

Rösel, A., L. Kaleschke, and G. Birnbaum, 2012: Melt ponds on Arctic sea ice determined from MODIS satellite data using an artificial neural network. *The Cryosphere*, **6 (2)**, 431–446, doi:10.5194/tc-6-431-2012.

Schröder, D., D. Feltham, D. Flocco, and M. Tsamados, 2014: September Arctic sea-ice minimum predicted by spring melt-pond fraction. *Nature Climate Change*, **4**, 353–357, doi:https://doi.org/10.1038/nclimate2203.

Serreze, M. C., A. D. Crawford, J. C. Stroeve, A. P. Barrett, and R. A. Woodgate, 2016: Variability, trends, and predictability of seasonal sea ice retreat and advance in the Chukchi Sea. *Geophys. Res. Lett.*, **121**, 7308– 7325, doi:10.1002/2016JC011977.

Serreze, M. C., M. M. Holland, and J. Stroeve, 2007: Perspectives on the Arctic's shrinking sea-ice cover. *Science*, **315 (5818)**, 1533–1536, doi:10.1126/science.1139426.

Simmonds, I., and I. Rudeva, 2018: The great Arctic cyclone of August 2012. *Geophys. Res. Lett.*, **39**, L23 709, doi:10.1029/2012GL054259.

Spreen, G., R. Kwok, and D. Menemenlis, 2011: Trends in Arctic sea ice drift and role of wind forcing: 1992–2009. *Geophys. Res. Lett.*, **38**, L19 501, doi:10.1029/2011GL048970.

Staalesen, A., 2017: 100 sailors trapped in ice near Arctic outpost. *The Barents Observer*, URL https://thebarentsobserver.com/en/arctic/2017/02/100-sailors-trapped-ice-near-arctic-outpost.

Steele, M., W. Ermold, and J. Zhang, 2008: Arctic Ocean surface warming trends over the past 100 years. *Geophys. Res. Lett.*, **35**, L02 614, doi:10.1029/2007GL031651.

Steffen, K., J. Key, D. Cavalieri, J. Comiso, P. Gloersen, K. S. Germain, and I. Rubinstein, 1992: The estimation of geophysical parameters using passive microwave algorithms.

Microwave Remote Sensing of Sea Ice, F. D. Carsey, Ed., Geophysical Monograph, Vol. 68, American Geophysical Union, Washington, DC, 201–231.

Stroeve, J., L. C. Hamilton, C. M. Bitz, and E. Blanchard-Wrigglesworth, 2014: Predicting September sea ice: Ensemble skill of the SEARCH Sea Ice Outlook 2008–2013. *Geophys. Res.Lett.*, **41**, 2411–2418, doi:10.1002/2014GL059388.

Stroeve, J. C., A. B. V. Kattsov, M. Serreze, T. T. Pavlova, M. Holland, and W. N. Meier, 2012: Trends in Arctic sea ice extent from CMIP5, CMIP3 and observations. *Geophys. Res.Lett.*, **39**, L16 502, doi:10.1029/2012GL052676.

Tschudi, M., W. Meier, and J. Stewart, 2019a: An enhancement to sea ice motion and age products. *The Cryosphere Discussions*, **2019**, 1–29, doi:10.5194/tc-2019-40, URL https://www.the-cryosphere-discuss.net/tc-2019-40/.

Tschudi, M., W. N. Meier, J. S. Stewart, C. Fowler, and J. Maslanik, 2019b: Polar Pathfinder Daily 25 km EASE-Grid Sea Ice Motion Vectors, Version 4. [indicate subset used]. *Boulder, Colorado USA. NASA National Snow and Ice Data Center Distributed Active Archive Center*, doi:https://doi.org/10.5067/INAWUWO7QH7B.[October,2019].

Tschudi, M. A., J. A. Maslanik, and D. K. Perovich, 2008: Derivation of melt pond coverage on Arctic sea ice using MODIS observation. *Remote Sens. Environ.*, **112**, 2605–2614, doi:10.1016/j.rse.2007.12.009,2008.

Wang, J., J. Zhang, E. Watanabe, M. Ikeda, K. Mizobata, J. Walsh, X. Bai, and B. Wu, 2009: Is the Dipole Anomaly a major driver to record lows in Arctic summer sea ice extent? *Geophys. Res. Lett.*, **36**, L05 706, doi:10.1029/2008GL036706.

Williams, J., B. Tremblay, R. Newton, and R. Allard, 2016: Dynamic Preconditioning of the Minimum September Sea-Ice Extent. *J. Clim.*, **29**, 5879–5891, doi:https://doi.org/10.1175/JCLI-D-15-0515.1.

Willmes, S., S. Adams, D. Schröder, and G. Heinemann, 2011: Spatio-temporal variability of polynya dynamics and ice production in the Laptev sea between the winters of 1979/80 and 2007/08. *Polar Research*, **30 (1)**, 5971, doi:10.3402/polar.v30i0.5971.

Woodgate, R. A., 2018: Increases in the Pacific inflow to the Arctic from 1990 to 2015 and insights into seasonal trends and driving mechanisms from year-round Bering Strait mooring data. *Progress in Oceanography*, **160**, 124–154, doi:10.1016/j.pocean.2017.12.007.

Woodgate, R. A., T. Weingartner, and R. Lindsay, 2010: The 2007 Bering Strait oceanic heat flux and anomalous Arctic sea-ice retreat. *Geophys. Res.Lett.*, **37**, 1, doi:https://doi.org/10.1029/2009GL041621.

Zhan, Y., and R. Davies, 2017: September Arctic sea ice extent indicated by June reflected solar radiation. *J. Geophys. Res. Atmos.*, **122**, 2194–2202, doi:10.1002/2016JD025819.

Appendix A

Table A.1: Uncertainties in Pearson correlation coefficients between June RSR and SIE, and the minimum SIE anomalies for the time period 2000-2018 for each Arctic peripheral sea. Uncertainties are calculated from a Bootstrap analysis of 1000 resampling of n = 19 elements.

	June RSR	June SIE
Beaufort	0.10	0.05
Chukchi	0.21	0.15
East Siberian	0.20	0.22
Laptev	0.07	0.09
Kara	0.09	0.08

Appendix B

Following Williams et al. (2016) and Brunette et al. (2019), we present a regional analysis of late winter Coastal Divergence (CD) for July 1, June 1 and May 1 forecast dates. CD is a proxy for ice thickness anomaly before the melt onset and a skillful predictor for the Laptev Sea and pan-Arctic. To this end, we present correlation coefficients between CD integrated from start week WX (W3 to W24) to forecast dates of July 1, June 1 and May 1 for all peripheral seas (see Figure B.1). The optimal start week WX for the Beaufort, Chukchi, East Siberian, Laptev and Kara seas is taken to be W12, W15, W5, W5 and W10, respectively, irrespective of the forecast date (see Table B.1).

Different seas are expected to be affected differently by late winter dynamical processes. For instance, in the Laptev Sea, where the ice flow is mostly offshore, CD as early as February is believed to have an impact on the following September SIE (Brunette et al., 2019). This is the time scale required to thermodynamically grow 1.0-1.2 m of ice, i.e. the climatological melt in a given summer (Nikolaeva and Sesterikov, 1970). In the Beaufort Sea, where the pack can periodically move towards or away from the coastline in late winter, sea ice thickness anomalies caused by coastal divergence that occurs mid-winter can be erased by a subsequent coastal convergence event. For this reason, dynamical processes that occur later in the winter are expected to govern the predictive skill in this sea. Regardless, CD was shown to have predictive skill of the minimum SIE. For instance, anomalous divergence in the ice pack in February and April in the Beaufort Sea in 2016 lead to an ice-free cover in the region the following summer (Babb et al., 2019). In the East Siberian Sea, off-shore ice motion is not obviously dominant over on-shore or parallel-to-the-shore ice motion (Kimura et al., 2013; Kwok, 2006; Miles and
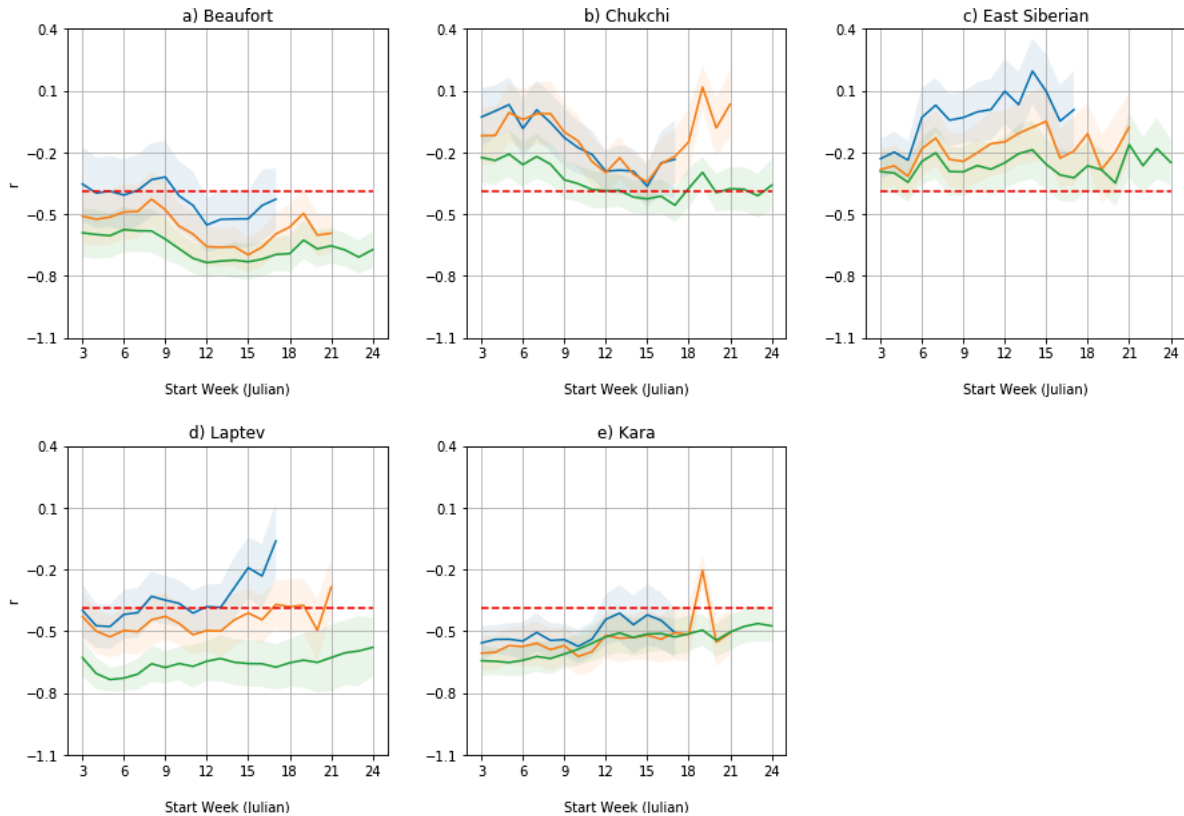
Figure B.1: Pearson correlation coefficients between late winter Coastal Divergence (CD) area anomalies integrated from start week WX (from W3 to W24 on x-axis) to July 1 (W24, green), June 1 (W21, orange) and May 1 (W18, blue) and minimum SIE anomalies. The red dashed line shows the 95% significance criteria for n = 26 elements. The shaded regions show the correlation uncertainties for each start week WX and each forecast date calculated from a Bootstrap analysis of 1000 resampling of n = 26 elements. The optimal start week WX that gives the peak correlation for each forecast date is chosen for each peripheral sea (see Table B.1).

Barry, 1998). On-shore ice motion erases the thin ice signal from the previous off-shore motion. For that reason, the peak correlation in CD is lost in spring, the signal is smaller and the correlation is significant at the 90% confidence level.

The maximum correlation between CD and the minimum SIE in the Laptev (-0.53) and Kara (-0.62) seas for a June 1 forecast are comparable to that of Williams et al. (2016), who finds a maximum correlation of –0.58 using a proxy for coastal divergence area anomalies estimated by backtracking a synthetic ice edge located at 77.5°N from June 1 until the 3rd week of April. The predictive skill was hypothesized to come from the Laptev Sea where offshore ice motion is a semi-permanent feature. This hypothesis was tested by

Brunette et al. (2019) who report a maximum correlation of -0.63 ∓ 0.1 for a May 1 forecast (compared to -0.48, ∓ 0.1 in this study) for a slightly larger Laptev Sea domain (70–85°N ,90–155°E) and a different time period of 1992-2016.

Table B.1: Start week (WX) for peak Pearson correlation coefficients between late winter coastal divergence area anomalies integrated from start week WX to July 1, June 1 and May 1 and the minimum SIE for each Arctic peripheral sea. The peak correlations are shown in parenthesis next to the given start week. Start week WX chosen for each peripheral sea is shown in bold. $|\Delta r|$ is the difference in the correlation coefficients between the chosen start week WX and start week WX with peak correlation when the two are different. $|\Delta r|$ is smaller than the computed correlation uncertainties for all peripheral seas (Figure B.1).

	Forecast Date			
	July 1	June 1	May 1	Chosen Start Week ($|\Delta r|$)
Beaufort	**W12 (-0.74)**	W15 (-0.70)	**W12 (-0.65)**	W12 (0.05)
Chukchi	W17 (-0.46)	**W15 (-0.34)**	**W15 (-0.36)**	W15 (0.03)
East Siberian	**W5/W20 (-0.34)**	**W5 (-0.32)**	**W5 (-0.24)**	W5 (0)
Laptev	**W5 (-0.73)**	**W5 (-0.53)**	**W5 (-0.48)**	W5 (0)
Kara	W5 (-0.65)	**W10 (-0.62)**	**W10 (-0.57)**	W10 (0.06)